High-statistics measurements of the $\bar{p}p \to \bar{\Lambda}\Lambda$ and $\bar{p}p \to \bar{\Lambda}\Sigma^0$+c.c. reactions at threshold

P. D. Barnes, G. Franklin, R. McCrady, F. Merrill, C. Meyer, B. Quinn, R. A. Schumacher, and V. Zeps
Carnegie-Mellon University, Pittsburgh, Pennsylvania 15260

N. Hamann*
CERN, CH-1211 Geneva, Switzerland

W. Eyrich, R. Geyer, J. Hauffe, M. Kirsch, R. A. Kraft, and F. Stinzing
Universität Erlangen-Nürnberg, D-91058 Erlangen, Germany

H. Fischer, J. Franz, E. Rössle, M. Ruh, H. Schmitt, and R. Todenhagen
Universität Freiburg, D-79104 Freiburg, Germany

K. Kilian, W. Oelert, K. Röhrich, K. Sachs, and T. Sefzick
Institut für Kernphysik des Forschungszentrums Jülich, D-52425 Jülich, Germany

B. D. Bunker, R. A. Eisenstein, P. G. Harris, D. W. Hertzog, T. D. Jones, and R. L. Tayloe
University of Illinois, Urbana, Illinois 61801

T. Johansson, S. Pomp, and E. Traneus
Uppsala University, S-75121 Uppsala, Sweden
(Received 5 June 2000; published 17 October 2000)

We report on precision measurements of the cross sections for the reactions $\bar{p}p \to \bar{\Lambda}\Lambda$, $\bar{p}p \to \bar{\Lambda}\Sigma^0$, and $\bar{p}p \to \bar{\Sigma}^0\Lambda$ in the region below 5 MeV excess kinetic energy above reaction threshold. For the $\bar{p}p \to \bar{\Lambda}\Lambda$ measurement, the data represent a third and definitive scan through the threshold region by this experiment. Improvements in the detector system and analysis techniques, coupled with greatly increased statistics, have negated the question of the existence of a near-threshold resonance as had been indicated in our earlier, lower-statistics studies. The high statistics permit the first extraction of the polarization information at these low energies. We also report the first measurement of the cross section for the complementary reactions $\bar{p}p \to \bar{\Lambda}\Sigma^0$+c.c. at excess energies up to 2.5 MeV. This allows a comparison of the onset of $\bar{\Lambda}\Lambda$ production to that of $\bar{\Lambda}\Sigma^0$ and $\bar{\Sigma}^0\Lambda$. The data show no evidence for near-threshold resonance structures in either reaction channel. Further, the $\bar{p}p \to \bar{\Lambda}\Sigma^0$+c.c. reactions exhibit a larger *P*-wave fraction close to threshold compared to $\bar{p}p \to \bar{\Lambda}\Lambda$.

PACS number(s): 25.43.+t, 13.75.Cs, 14.20.Jn

I. INTRODUCTION

The PS185 experiment at the Low-Energy Antiproton Ring (LEAR) was focused on a systematic study of antihyperon-hyperon ($\bar{Y}Y$) production reactions in the kinematic region from threshold to nearly 200 MeV excess energy. As part of this program, a special emphasis was made on obtaining data very near threshold for the $\bar{p}p \to \bar{\Lambda}\Lambda$ and $\bar{p}p \to \bar{\Lambda}\Sigma^0$+c.c. reactions.[1] At excess energies, $\epsilon = \sqrt{s} - m_Y - m_{\bar{Y}}$, below 5 MeV the reactions proceed through the lowest partial waves, essentially *S* and *P* waves. Theoretical descriptions are, in that respect, simpler in this region than at higher energies. The $\bar{\Lambda}\Lambda$ threshold region was studied twice previously by our collaboration [1,2]. The data featured a strong *P*-wave contribution which is usually interpreted as a consequence of the greater suppression of the *S* waves because of the strong annihilation in the *S* wave [3]. Alternatively, the existence of quasinuclear bound states in the $\bar{Y}Y$ system was also proposed as a means to explain the strong observed *P* wave [4]. A detailed study of the shape of the excitation function should reveal a structure if such an intermediate state is an important part of the dynamics of the production process. Indeed, in both prior measurements, the excitation function indicated a slight irregularity near $\epsilon = 0.8$ MeV with a combined statistical significance of approximately 2.3 standard deviations. The nature of the shape fueled speculations of the existence of a subthreshold quasinuclear $\bar{\Lambda}\Lambda$ *D*-wave state [5]. This irregularity was the principal motivation to revisit the near-threshold region with higher integrated luminosity and using a detector and measurement procedure optimized for such a threshold scan.

Additionally, we have studied the complementary channels $\bar{p}p \to \bar{\Lambda}\Sigma^0$+c.c. very close to threshold to scan for evi-

*Deceased.

[1]Here c.c. denotes the charge-conjugate state $\bar{\Sigma}^0\Lambda$. We use the shorthand notation $\bar{\Lambda}\Sigma^0$ throughout the document to represent $\bar{\Lambda}\Sigma^0 + \bar{\Sigma}^0\Lambda$.

dence of similar structures and to examine the production dynamics in this related system. Comparison of $\overline{\Lambda}\Lambda$ and $\overline{\Lambda}\Sigma^0$ at the same excess energy is a means to test proposed reaction mechanisms. The $(\overline{\Lambda}\Sigma^0+\overline{\Sigma}^0\Lambda)/\overline{\Lambda}\Lambda$ cross section ratio, measured at excess energies from 15 to 39 MeV, was found [6,7] to be approximately 0.27. This ratio is in line with theoretical predictions [9,10] and is consistent with data at significantly higher energies [8]. It is of interest to test the validity of these predictions closer to threshold because differences would give additional information about the reaction mechanism and/or differences in the final-state interaction (FSI).

A brief outline of the experiment and general analysis procedure is given next, followed by details of special interest to the threshold analyses. Two independent analyses were made on the high-statistics $\overline{\Lambda}\Lambda$ data. Both are in excellent agreement with one another and in moderate disagreement with our previous work. The interpretation of this is discussed. The $\overline{\Lambda}\Sigma^0$ experiment was technically quite similar to the $\overline{\Lambda}\Lambda$ measurement, however several key analysis differences were employed which are described below.

II. EXPERIMENT

The PS185 detector shown in Fig. 1 consists of four main parts: target, decay spectrometer, triggering system, and baryon identification system. The proton target is constructed from four individual polyethylene (CH_2) cylindrical cells (2.5 mm radius and length). The hydrogen nuclei in the hydrocarbon chain serve as the source of free protons. A 1.5 mm long pure carbon cell is placed immediately upstream in order to determine the number of background events generated by the presence of carbon nuclei. The discrete nature of the target serves two purposes. First, the four cells combined form a thick target, thus increasing the number of $\overline{p}p$ interactions while retaining position and energy bin information. Second, the CH_2 and the pure carbon cell each lower the beam energy by $\approx$0.25 MeV which facilitates a continuous cross section scan in small steps for a given beam momentum. Additionally, an external degrader was used whose energy loss corresponds to two target cells. Data were obtained for each LEAR momentum setting, with and without the degrader. In this manner each excess energy setting was surveyed twice with the origin of events for a given value of ϵ from different target cells.

The LEAR extracted antiproton beam has a relative momentum spread of approximately 10^{-4} rms which translates to a negligible distribution in the average momentum compared to the straggling in an individual target cell. However, the real beam momentum spread is considerably larger due to statistical fluctuations in the energy loss by passing through vacuum windows, timing counters, and a multiplane silicon microstrip system, all upstream of the target cells. The average momentum of the antiprotons exiting the LEAR machine was tuned to experimental specification with an accuracy of approximately 1 MeV/c. This translates to an uncertainty in the absolute scale of the excess energy of approximately 350 keV. The final absolute energy scale was

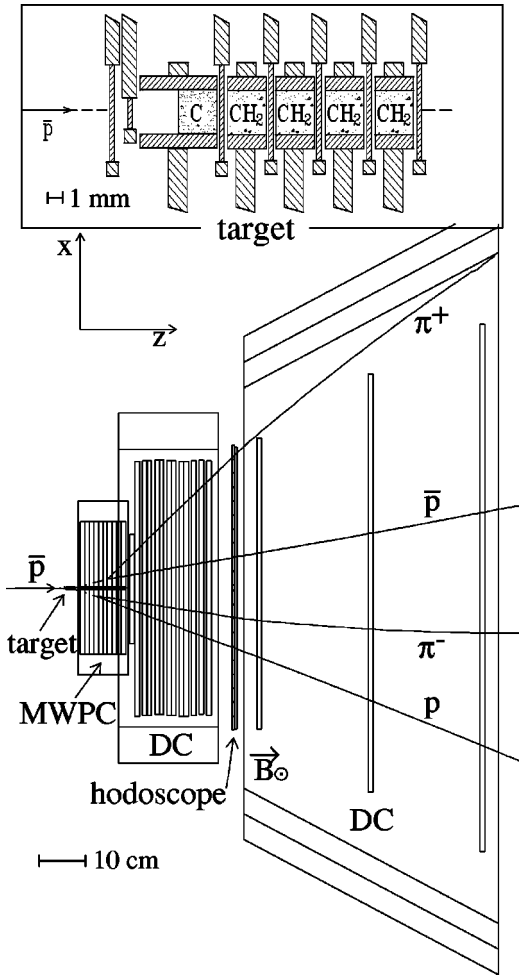

FIG. 1. Schematic view of the PS185 detector and target system. Hyperon-antihyperon pairs are created in one of five segmented target cells. The scintillator hodoscope and the detectors surrounding the target cells are used to form appropriate triggers. Proportional chambers (MWPC) and drift chambers (DC) are used to detect the characteristic decay V^0 patterns from neutral hyperon decays. The drift chambers in the magnet enable the sign of the charged tracks to be determined.

determined by an offline procedure described below.

The $\overline{\Lambda}\Lambda$ measurement was made in one continuous run at LEAR using six momentum settings to span the excess energy range $\epsilon_{\overline{\Lambda}\Lambda}$ from 0.0 to 5.0 MeV. With the multicell target and degraders, 30 independent cross section measurements were obtained using a total of 4.2×10^{11} antiprotons. The $\overline{\Lambda}\Sigma^0$ data set comprised four momentum settings obtained in two running periods. A total of 3.5×10^{11} antiprotons were used. The actual delivered momenta covered an effective range from -1.0 to 2.5 MeV in $\epsilon_{\overline{\Lambda}\Sigma^0}$ with nearly 43% of the recorded integrated luminosity below threshold. The relatively large data sample just below $\overline{\Lambda}\Sigma^0$ threshold was used to compute the level of background events which leak into the $\overline{\Lambda}\Sigma^0$ sample from carbon events and from the dominant $\overline{\Lambda}\Lambda$ reaction.

In the $\overline{\Lambda}\Lambda$ and $\overline{\Lambda}\Sigma^0$ threshold studies, the emitted hyperons reside within a cone of less than 6° about the beam axis.

For the $\bar{p}p \to \bar{\Lambda}\Sigma^0 +$ c.c. reactions the Σ hyperon decays immediately to $\Lambda\gamma$ giving the Λ a momentum kick of approximately 77 MeV/c. The γ is unmeasured. Thus for both reactions studied we measure $\bar{\Lambda}\Lambda$ pairs which are observed through their charged decay mode, $\bar{p}\pi^+$ and $p\pi^-$, with a product branching fraction of 40.8%. To reconstruct these events, excellent knowledge of the incoming antiproton direction is required and to do this each incoming $\bar{p}$ is measured to an angular precision of 1.64 mrad using a set of silicon microstrip detectors. The charged decay $\Lambda \to p\pi^-$ is reconstructed in a series of ten proportional and 13 drift chamber planes immediately downstream of the targets. The center wire is made insensitive over a 6 mm central segment of the proportional chambers and a 9 mm segment in the drift chambers to permit the noninteracting antiproton beam to pass unrecorded. A correct modeling and treatment of this insensitive region is very important for these threshold data.

Successfully reconstructed events from either reaction include two isolated decay vertices (V^0 events). In all cases, kinematics constrain the decay proton and antiproton to a forward cone which is entirely intercepted by a vertically oriented magnetic field containing three additional drift chambers. The left-right deflection of the baryons in the magnet is used to produce a Λ or $\bar{\Lambda}$ tag for each decay vertex.

The electronic trigger is straightforward. An antiproton arriving at a target cell is registered by a series of upstream scintillators. A signal from a neutral reaction is obtained when this antiproton enters a cell and the scintillators immediately downstream and surrounding the cell do not fire. A candidate $\bar{Y}Y$ event is defined as the neutral reaction in coincidence with two or more charged particles firing a segmented scintillator hodoscope which is placed downstream of the chambers to intercept all of the decay baryons. In practice five parallel triggers exist; each is associated with a specific target cell. A small electromagnetic calorimeter array placed downstream of the magnet was used in one of the analysis efforts to normalize the neutral trigger rates coming from different cells. The $\bar{p}p \to \bar{n}n$ reaction has a high probability of producing an antineutron which, upon entering the calorimeter, annihilates and deposits a large amount of energy. No structure is expected in this cross section over the small range of momentum studied here. The rate of events of this type from cell to cell and from momentum setting to momentum setting constitutes a reliable method of ensuring that the neutral target cell component of the trigger was stable and evenly balanced.

III. DATA ANALYSIS

The philosophy of the data analysis procedure is largely similar to previous descriptions (e.g., Ref. [7]) although the detailed implementations differed significantly. Tracks are reconstructed from the hit distribution in the wire planes. Candidate V^0 patterns are assembled from two tracks with a common vertex. Events with one or several pairs of acceptable V^0 formations are presented to a kinematical fit to test the $\bar{p}p \to \bar{\Lambda}\Lambda \to \bar{p}\pi^+ p\pi^-$ hypothesis. In the case of the $\bar{\Lambda}\Sigma^0$ analysis, a separate fit is made to each of the three possible event types $\bar{\Lambda}\Sigma^0$, $\bar{\Sigma}^0\Lambda$, and $\bar{\Lambda}\Lambda$. The assignment of event type is based on the solution with the lowest χ^2 per degree of freedom.

Proximity to threshold introduces special considerations because the phase space is rapidly collapsing as the threshold is approached. Uncertainties in the LEAR beam momentum, momentum straggling due to upstream energy losses, and finite resolution in the tracking system complicate the event identification process. These effects exaggerate the fact that, as threshold is approached, the mapping of the laboratory angles to the center-of-mass production angles for the produced hyperons becomes ambiguous. A GEANT-based [11] Monte Carlo simulation was used to completely describe the detector system and to determine the proper acceptance function for each reaction and excess energy. Monte Carlo studies determined the differential binning which could be used reliably for each excess energy in the $\bar{p}p \to \bar{\Lambda}\Lambda$ reaction.

For the $\bar{p}p \to \bar{\Lambda}\Sigma^0 +$ c.c. reactions, the proximity to threshold causes especially severe problems because the background from the abundant $\bar{\Lambda}\Lambda$ events is very large. Even at the highest $\bar{\Lambda}\Sigma^0$ excess energy point studied ($\epsilon = 2.5$ MeV), the $\bar{\Lambda}\Lambda$ cross section is 40 times greater than $\bar{p}p \to \bar{\Lambda}\Sigma^0 +$ c.c. Simulations showed that a reliable distinction between $\bar{\Lambda}\Sigma^0$ and $\bar{\Sigma}^0\Lambda$ is not possible this close to threshold [12]. Hence, we do not report separate cross sections for the two charge-conjugate reactions. This also means that the reconstrucion of the center-of-mass reaction angle is ambiguous for these reactions and no differential cross sections are therefore reported.

The momentum of each data point was first estimated from the value stated by LEAR, corrected for known energy losses in material upstream of the target cells. The final value was obtained with an iterative procedure which makes use of the kinematic fit. A pure sample of the highest-quality $\bar{\Lambda}\Lambda$ events[2] was obtained, which would be certain to be identified correctly whether or not the assumed momentum was correct, within reasonable bounds. These events were then refit with the beam momentum treated as an unconstrained variable and a new beam momentum was obtained as the mean of the post-fit values. The iterations converged rapidly. The procedure was subjected to numerous tests which resulted in the determination of the rms uncertainty on the mean momentum of 0.20 MeV/c for the $\bar{\Lambda}\Sigma^0$ data and 0.15 MeV/c for $\bar{\Lambda}\Lambda$ data. A Monte Carlo simulation was used to calculate the momentum spread for each target cell, the width of which is typically 0.78 MeV/c with a central value skewed toward lower momenta. All reported observables are averages over such a distribution.

Two methods were used to determine the level of background in the final event samples. The number of events that can be attributed to hyperon-antihyperon production on the

[2]For the $\bar{\Lambda}\Sigma^0$ study, the $\bar{\Lambda}\Lambda$ events are plentiful and well above threshold.

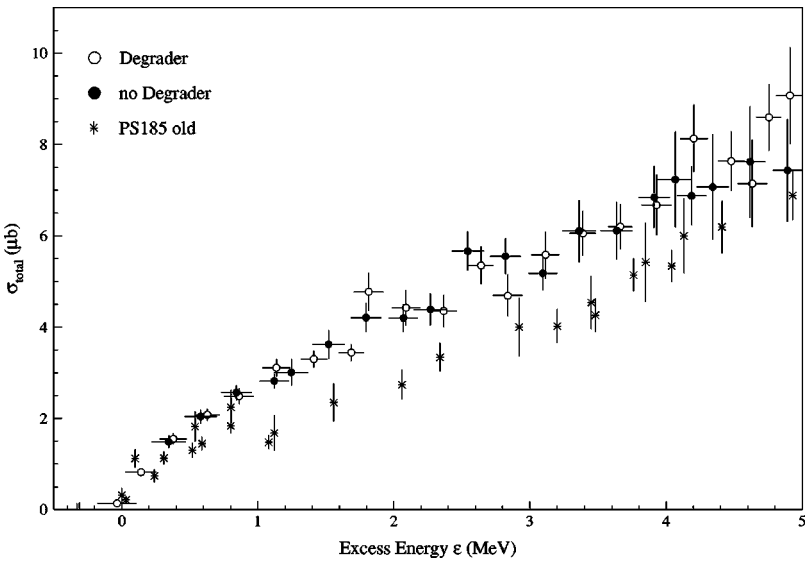

FIG. 2. Total cross section results for the $\bar{p}p \rightarrow \bar{\Lambda}\Lambda$ reaction versus excess kinetic energy above reaction threshold. The open and solid circles correspond to data obtained with the degrader in and out, respectively, for the data reported here. The crosses are the earlier PS185 results.

carbon nuclei of the target cells was determined by counting events produced in the pure carbon target which pass all kinematic cuts. For both the $\bar{\Lambda}\Lambda$ and $\bar{\Lambda}\Sigma^0$ measurements, this represents an approximately 4–5 % contamination of the final event sample and the fraction is relatively independent of excess energy. The final cross sections are corrected for this background.

In both threshold experiments, a fraction of the data was obtained below threshold. These data were analyzed in the same manner as described above however the antiproton momentum was permitted to vary in the kinematic fitter starting from an initial artificially high ''above threshold'' value. Events of the right geometrical topology, but wrong physical origin, could be misinterpreted by the kinematic fit, allowing an estimation of such contamination. In the case of $\bar{\Lambda}\Lambda$, no events were found beyond the level expected from, and accounted for, by the carbon component of the target cells.

The large data set which lies 0 to 4 MeV/c below threshold for the $\bar{\Lambda}\Sigma^0$ measurement is certain to contain no free $\bar{\Lambda}\Sigma^0$ events. It does feature a significant number of $2V^0$ candidates because of the large $\bar{\Lambda}\Lambda$ cross section ($\approx$66 μb). We used this data set to determine simultaneously the carbon-induced and $\bar{\Lambda}\Lambda$ contamination fraction which were misidentified as $\bar{\Lambda}\Sigma^0$. The comparative study of the $\bar{\Lambda}\Sigma^0$ along with the $\bar{\Lambda}\Lambda$ events further reduces systematic uncertainties on the $\bar{\Lambda}\Sigma^0$ results as long as the final results are reported as the ratio $\sigma(\bar{\Lambda}\Sigma^0+\bar{\Sigma}^0\Lambda)/\sigma(\bar{\Lambda}\Lambda)$. The absolute cross section $\sigma(\bar{\Lambda}\Sigma^0+\bar{\Sigma}^0\Lambda)$ is then obtained by multiplying the measured ratio by an empirical $\sigma(\bar{\Lambda}\Lambda)$ function obtained by fitting a polynomial to the global PS185 $\bar{\Lambda}\Lambda$ data set. The major different systematic uncertainty which remains is due to the insensitive central region of the decay spectrometer. This has a slightly different effect on near-threshold ($\bar{\Lambda}\Sigma^0$) events compared to above-threshold ($\bar{\Lambda}\Lambda$) events due to the kinematics differences. A careful study of this effect was performed resulting in a 2% relative uncertainty in the cross-section scaling which is included in the assigned errors.

IV. RESULTS AND DISCUSSION

A. The $\bar{p}p \rightarrow \bar{\Lambda}\Lambda$ reaction

Two independent evaluations of the $\bar{\Lambda}\Lambda$ data were made in order to reduce any analysis-dependent systematic biases. Both procedures [13] followed essentially the scheme described above, however, details differed. The final agreement between the two efforts for the total cross section determination is excellent. The only difference is a small variance in the differential cross sections at extreme forward angles. This is associated with the treatment of the insensitive region of the proportional chambers and was included in the systematical uncertainty. We used the two procedures to estimate the range of this uncertainty and folded this error into our statistical errors for the reported differential and total cross sections. The differential polarization data are free from this effect.

The total cross section results are shown in Fig. 2. The open and solid circles correspond to the data obtained with the degrader in and out, respectively. The excellent agreement provides evidence that our redundant procedure of measuring each excess energy with two different target cells works well. Figure 2 also includes the results of the earlier PS185 studies [1,2] for comparison. The inflection in the earlier data close to $\epsilon = 0.8$ MeV is not evident in the new results. Furthermore, above 1 MeV, the earlier data lie consistently below the new results. We return to both of these points in the discussion.

The energy dependence of the total cross section could be fit to a simple model [14,15]. In this model, the scattering lengths, as is customary, are independent of energy. In addition, the model assumes that the initial- and final-state interactions do not vary significantly over the first 5 MeV above threshold. Therefore the shape of the excitation function is given by the phase space behavior of the participating partial waves. This close to threshold one can safely assume that, at most, partial waves up to $\ell = 2$ may contribute. The total cross section can then be written

$$\sigma_T = \frac{2\pi q}{ps}(m_p m_\Lambda)^2(a_S + a_P q^2 + a_D q^4). \qquad (1)$$

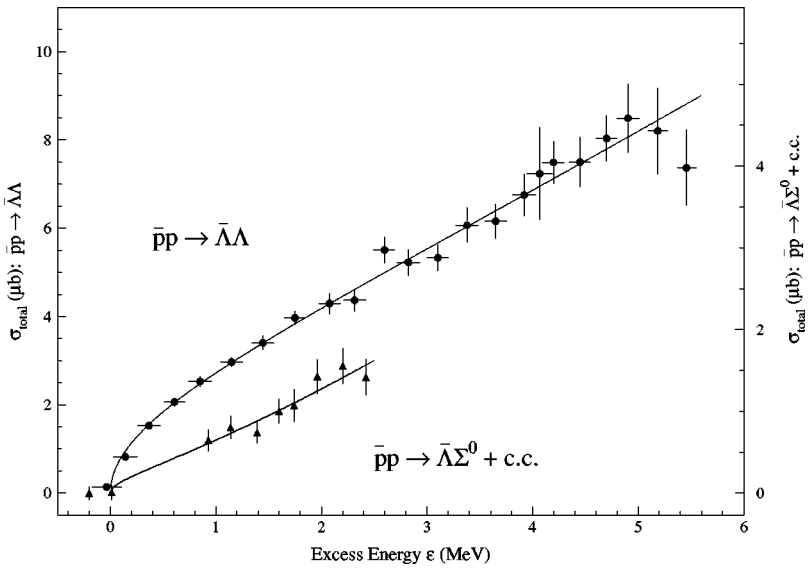

FIG. 3. Final total cross section results for the $\bar{p}p \to \bar{\Lambda}\Lambda$ reaction (left ordinate, upper curve) and the $\bar{p}p \to \bar{\Lambda}\Sigma^0$ + c.c. reactions (right ordinate, lower curve) versus excess kinetic energy above respective threshold. The data are fit to the near-threshold parametrization $\sigma_T = c_S \epsilon^{1/2} + c_P \epsilon^{3/2}$ as described in the text.

Here p and q denote the center-of-mass (c.m.) momenta of the incoming antiproton and the outgoing hyperons, respectively, and s is the total energy of the c.m. squared. The coefficients a_S, a_P, and a_D represent the S-, P-, and D-wave contributions and can be related to the scattering lengths [14]. Furthermore, $q \propto \epsilon^{1/2}$ so that the above expression can be rewritten as a polynomial relation

$$\sigma_T = c_S \epsilon^{1/2} + c_P \epsilon^{3/2} + c_D \epsilon^{5/2}. \tag{2}$$

Fitting the total cross section points with Eq. (2) yields the result that the inclusion of the D-wave term does not improve significantly the fit compared to using S and P waves only. A fit with the D-wave coefficient set to zero, yields $c_S = 2.49 \pm 0.07$ and $c_P = 0.24 \pm 0.03$, each in appropriate units, with a $\chi^2/N_{\mathrm{DF}} = 13.1/20$. This fit is shown as the solid line through the $\bar{\Lambda}\Lambda$ data points in Fig. 3. Two remarks are in order. First, the very good fit to the two-term expression indicates that there are no significant contributions of D waves this close to threshold (subject to the above assumptions). More importantly, there is no need to include any resonant structure in the excitation function. These data strongly restrict the possibility of a quasinuclear $\bar{N}N$ bound state near to the $\bar{\Lambda}\Lambda$ threshold. Table I lists the final total cross section data for the $\bar{p}p \to \bar{\Lambda}\Lambda$ reaction. The statistical and systematic errors are listed separately. An additional global uncertainty on the cross section scale from overall normalization considerations is approximately 5%.

Comparing the new results to previous PS185 findings [1,2] gives the impression that the current experiment is in disagreement with previous reported results. However, the apparent difference in the cross section scale is largely accounted for by the fact that the overall normalization uncertainty in the earlier experiments was estimated to be approximately 15%. The largest component of this uncertainty was the acceptance function used in the analysis of the earlier data which was based on an incomplete (pre-GEANT) Monte Carlo. In particular, the hadronic interaction correction used then is now known to have underestimated the true correction leading to an upward adjustment of older data by approximately 8–12 %. With these global normalization considerations, the two data sets are more closely compatible. Still, there remains a difference in the observed P-wave fraction; the new data which features high-statistical precision in the differential cross section results, requires a smaller P-wave fraction compared to the earlier results.

TABLE I. Final total cross section results for the $\bar{p}p \to \bar{\Lambda}\Lambda$ reaction. The first error on the cross section is statistical and the second is systematic. The uncertainty on ϵ represents the bin width of the included data.

ϵ (MeV)	$\sigma_{\mathrm{tot}}(\mu\mathrm{b})$
-0.035 ± 0.141	$0.141 \pm 0.031 \pm 0.023$
0.142 ± 0.113	$0.821 \pm 0.086 \pm 0.041$
0.365 ± 0.109	$1.527 \pm 0.086 \pm 0.057$
0.609 ± 0.102	$2.060 \pm 0.099 \pm 0.077$
0.852 ± 0.110	$2.527 \pm 0.116 \pm 0.082$
1.150 ± 0.107	$2.971 \pm 0.099 \pm 0.090$
1.448 ± 0.103	$3.407 \pm 0.159 \pm 0.121$
1.749 ± 0.101	$3.970 \pm 0.154 \pm 0.110$
2.079 ± 0.104	$4.293 \pm 0.239 \pm 0.152$
2.315 ± 0.110	$4.369 \pm 0.251 \pm 0.156$
2.594 ± 0.103	$5.504 \pm 0.294 \pm 0.216$
2.826 ± 0.111	$5.229 \pm 0.297 \pm 0.199$
3.102 ± 0.104	$5.333 \pm 0.299 \pm 0.220$
3.379 ± 0.106	$6.069 \pm 0.396 \pm 0.234$
3.652 ± 0.102	$6.162 \pm 0.389 \pm 0.217$
3.921 ± 0.110	$6.757 \pm 0.474 \pm 0.275$
4.067 ± 0.123	$7.234 \pm 1.044 \pm 0.378$
4.196 ± 0.104	$7.491 \pm 0.487 \pm 0.282$
4.448 ± 0.101	$7.504 \pm 0.566 \pm 0.317$
4.699 ± 0.099	$8.038 \pm 0.523 \pm 0.321$
4.904 ± 0.103	$8.491 \pm 0.782 \pm 0.397$
5.185 ± 0.096	$8.205 \pm 0.974 \pm 0.502$
5.460 ± 0.090	$7.374 \pm 0.857 \pm 0.375$

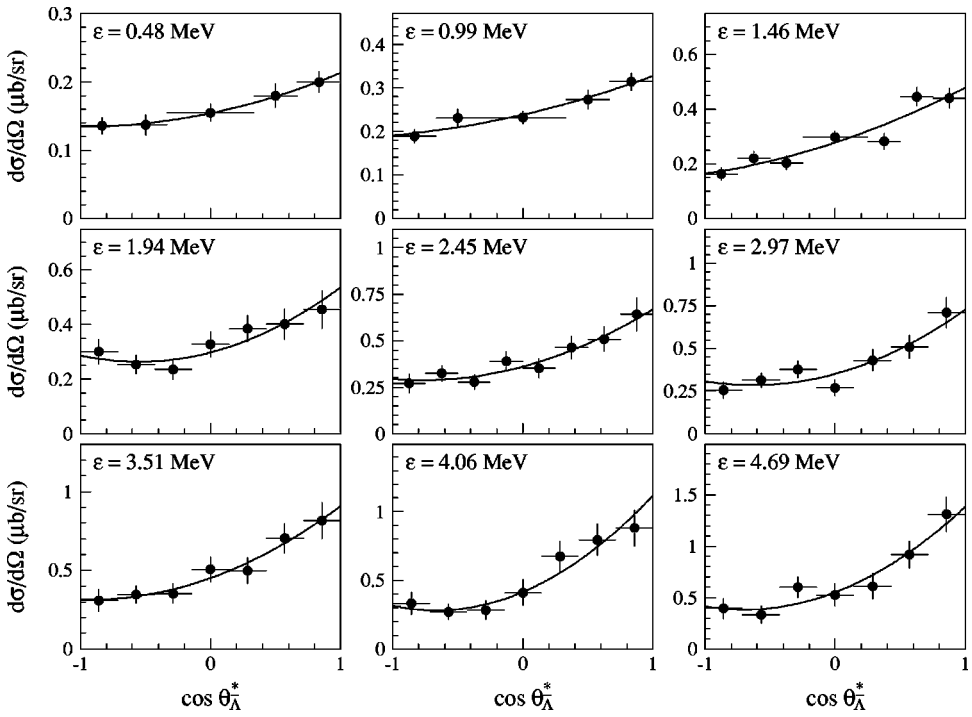

FIG. 4. Differential cross section results for $\bar{p}p \to \bar{\Lambda}\Lambda$ for nine excess energy groupings. Curves through the data represent fits using a second-order Legendre expansion.

Differential cross sections are evaluated for nine energy binnings of the data and are shown in Fig. 4. The quality of the data illustrates the onset of P waves with unprecedented resolution. With Θ^* defined as the center-of-mass scattering angle of the emitted anti-lambda, the Legendre polynomial expansion

$$\frac{d\sigma}{d\Omega}(\Theta^*) = \sum a_n P_n(\cos\Theta^*), \tag{3}$$

is used to fit the data. The results are included in the figures and the coefficients are plotted versus excess energy in Fig. 5. A smooth turn on of the partial waves is evident and the importance of the S- and P-wave interference is made clear from the sizable a_1 coefficient.

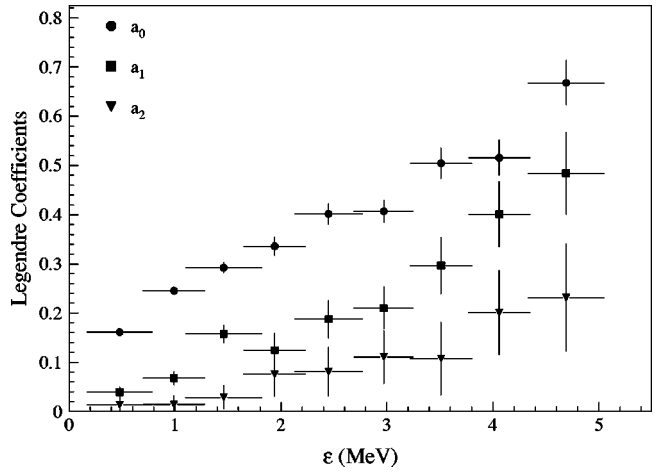

FIG. 5. Legendre coefficients for fits to the $\bar{p}p \to \bar{\Lambda}\Lambda$ differential cross section curves shown in Fig. 4.

The parity-violating weak decay is exploited to determine the polarization of the emitted hyperons which is defined to be the average of P_y^{Λ} and $P_y^{\bar{\Lambda}}$. The $\hat{y}$ direction is normal to the production plane. In our earlier studies at higher energy, the high-statistics data sets [16,17] identified a trend in the differential polarization curves [18]. In general, the sign of the polarization is dependent on t', where $t' \equiv t - t_{\min} = 2pq(\cos\Theta^* - 1)$ is the reduced four-momentum transfer (squared) and p and q are the incoming and outgoing c.m. momenta, respectively. The lambda and anti-lambda polarization is positive for $|t'|$ below 200 $(\mathrm{MeV}/c)^2$. At $|t'| \approx 200$ $(\mathrm{MeV}/c)^2$, the polarization crosses zero and becomes negative as $|t'|$ increases. All of the data reported here are in a range with $|t'| < 150$ $(\mathrm{MeV}/c)^2$ and they are plotted in Fig. 6 together with fits using associated Legendre polynomials

$$P = \sum b_n P_n^1(\cos\Theta^*). \tag{4}$$

The associated polynomials are used because at forward and backward c.m. angles, the reaction plane disappears, leaving the polarization undefined. The coefficients of the fits are given in Table II. All differential polarization curves are positive over the allowed c.m. angular range. The data, binned in four excess energy groups, are the first to demonstrate experimentally the large positive polarization anticipated for small excess energies when extrapolating from the higher-energies findings.

B. The $\bar{p}p \to \bar{\Lambda}\Sigma^0$ + c.c. reactions

The $\bar{p}p \to \bar{\Lambda}\Sigma^0$ + c.c. data set spanned excess energies up to 2.5 MeV. The total cross section results are listed in Table III. The measurement made here is actually the ratio of cross

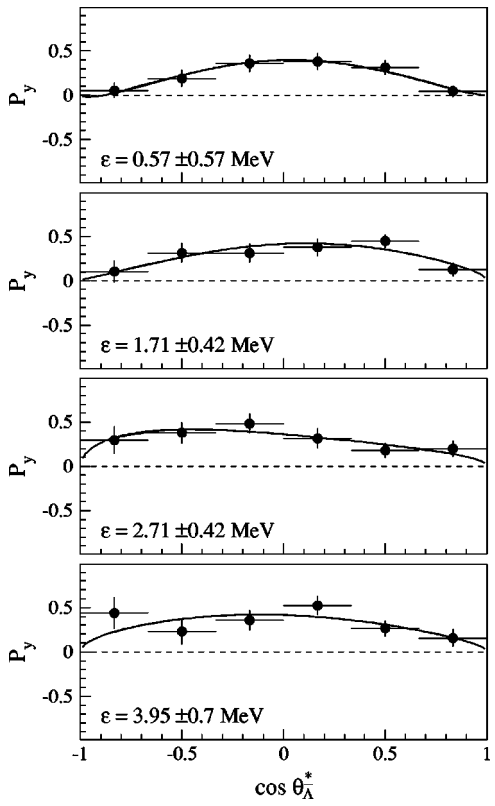

FIG. 6. Differential polarization results for $\bar{p}p \to \bar{\Lambda}\Lambda$. The positive polarization for all plots is consistent with expectations based on the trends of the global PS185 polarization data when represented versus t', the reduced four-momentum transfer squared. The solid curves are fits using associated Legendre polynomials.

sections $r = \sigma(\bar{p}p \to \bar{\Lambda}\Sigma^0 + \text{c.c.})/\sigma(\bar{p}p \to \bar{\Lambda}\Lambda)$ for the same incoming antiproton momentum. In order to obtain the absolute cross section, we have multiplied r by an empirical fit to the global PS185 data. These results are plotted in Fig. 3 and correspond to the cross section scale listed on the right ordinate. The same fitting procedure described above [see Eq. (2)] was applied yielding coefficients $c_S = 0.39 \pm 0.17$ and $c_P = 0.25 \pm 0.10$ in appropriate units. The fit is shown as the solid line through the triangular data points. The uncertainty is relatively large; the *P*- to *S*-wave ratio can range from 1/3 to 1 within the errors but it is clear that the relative *P*-wave contribution near threshold for this reaction is significantly larger than for the $\bar{\Lambda}\Lambda$ case. Over this limited region no additional structure is necessary to describe the excitation function. Similar to the $\bar{p}p \to \bar{\Lambda}\Lambda$ reaction, the $\bar{\Lambda}\Sigma^0$ cross section appears to turn on smoothly.

TABLE II. Coefficients of the associated Legendre polynomial fits to the differential polarization data. Four excess energy bins have been used. The central value is given with the uncertainty representing the range of included data.

ϵ (MeV)	b_1	b_2	b_3
0.57 ± 0.59	0.4240 ± 0.0020	0.0252 ± 0.0038	0.0111 ± 0.0048
1.71 ± 0.42	0.5300 ± 0.0028	0.0340 ± 0.0052	0.0082 ± 0.0068
2.71 ± 0.42	0.5510 ± 0.0033	0.0455 ± 0.0061	0.0160 ± 0.0077
3.95 ± 0.70	0.7010 ± 0.0040	0.0523 ± 0.0077	0.0169 ± 0.0097

TABLE III. Results of $\bar{\Lambda}\Sigma^0$ cross section analysis. The ratio $\sigma(\bar{p}p \to \bar{\Lambda}\Sigma^0 + \text{c.c.})/\sigma(\bar{p}p \to \bar{\Lambda}\Lambda)$ is the result of this analysis. The total cross section $\sigma(\bar{p}p \to \bar{\Lambda}\Sigma^0 + \text{c.c.})$ is determined from a simple polynomial fit to the global PS185 $\sigma(\bar{\Lambda}\Lambda)$ data.

ϵ (MeV)	$\sigma(\bar{p}p \to \bar{\Lambda}\Sigma^0 + \text{c.c.})$ (μb)	$\sigma(\bar{p}p \to \bar{\Lambda}\Sigma^0 + \text{c.c.})/\sigma(\bar{p}p \to \bar{\Lambda}\Lambda)$
-0.20	0.000 ± 0.079	0.0000 ± 0.0012
0.01	0.010 ± 0.091	0.0002 ± 0.0014
0.93	0.646 ± 0.134	0.0098 ± 0.0020
1.14	0.805 ± 0.139	0.0122 ± 0.0020
1.39	0.741 ± 0.131	0.0112 ± 0.0019
1.60	1.002 ± 0.148	0.0151 ± 0.0021
1.74	1.071 ± 0.201	0.0161 ± 0.0030
1.96	1.426 ± 0.209	0.0214 ± 0.0030
2.20	1.557 ± 0.218	0.0234 ± 0.0031
2.42	1.417 ± 0.218	0.0212 ± 0.0031

The comparison of the $\bar{\Lambda}\Sigma^0$ to $\bar{\Lambda}\Lambda$ cross sections at the same excess energies reduces phase space differences and provides information on the production dynamics and on the final-state interaction differences between these otherwise very similar reactions. At the excess energies 15, 26, and 39 MeV, we found the ratio

$$\frac{\sigma(\bar{\Lambda}\Sigma^0 + \bar{\Sigma}^0\Lambda)/2}{\sigma(\bar{\Lambda}\Lambda)} = \frac{\sigma(\bar{\Lambda}\Sigma^0)}{\sigma(\bar{\Lambda}\Lambda)} \simeq 0.27 \qquad (5)$$

in agreement with several theoretical estimates [9,10] based on one-boson exchange (OBE) models. Our conclusion was that the ratio of cross sections ''appears to be independent of energy in the low-energy regime studied here'' [7]. The ordinate scales in Fig. 3 for $\bar{\Lambda}\Sigma^0$:$\bar{\Lambda}\Lambda$ cross sections are in the ratio (0.27×2):1 to reflect this anticipated ratio. The factor of 2 is present because the $\bar{\Lambda}\Sigma^0$ data are plotted as the *sum* of the two independent reactions $\bar{\Lambda}\Sigma^0$ and $\bar{\Sigma}^0\Lambda$. Had the ratio remained constant near threshold, the $\bar{\Lambda}\Sigma^0$ data would lie on top of the $\bar{\Lambda}\Lambda$ data in the figure. A clear deviation is seen; the ratio drops by nearly a factor of 2.

In a typical OBE model [9,10] the $\bar{\Lambda}\Sigma^0$ channel is more strongly coupled to K^* exchange compared to the $\bar{\Lambda}\Lambda$ channel. This fact suggests that the $\bar{\Lambda}\Sigma^0$ reaction takes place at shorter distances which should, in turn, lead to an earlier onset of higher partial waves and differences in the FSI near threshold. A short-range production process would be expected to yield a smaller cross section because of increased FSI. This would be especially true near threshold where the relative hyperon momenta is small. At threshold, we observe that the *P*- to *S*-wave ratio for $\bar{\Lambda}\Sigma^0$ production is higher by a factor of at least 3 compared to $\bar{\Lambda}\Lambda$. The greater *P*-wave component suggests possible direct evidence for K^* ex-

change. The fact that the ratio of total cross sections ($\bar{\Lambda}\Sigma^0/\bar{\Lambda}\Lambda$) increases from threshold over the first 15 MeV to an asymptotic value of about 0.27 further supports the inference of a greater role of the FSI near threshold compared to at higher excess energies.

V. SUMMARY

We have completed a final study at LEAR of the threshold region for the reaction $\bar{p}p \to \bar{\Lambda}\Lambda$ with the specific aim of using the increased beam flux and improved detector setup to look for confirmation of earlier evidence of a structure in the total cross section. No structure is seen in these new measurements. The cross section is observed to grow smoothly from threshold with a mix of *S*- and *P*-wave production. The high statistics of this data set compared to our previous work greatly improves the differential cross section data available near threshold. The characteristic forward peaking of the differential cross section which dominates the reaction at higher excess energies is seen to evolve from this very-near threshold data, although the observed *P*-wave fraction here is smaller compared to our earlier findings. Finally, the first observation of the differential polarization in the threshold region is given. It is positive over the whole kinematic range, consistent with extrapolation from higher-energy PS185 studies.

We also report, for the first time, the results of a study of the complementary reactions $\bar{p}p \to \bar{\Lambda}\Sigma^0 + \text{c.c.}$ near threshold. The cross section strength compared to the $\bar{\Lambda}\Lambda$ reaction at the same excess energies differs from previous comparisons at significantly higher excess energies. The onset of this reaction indicates a three-times higher contribution of *P* waves compared to the $\bar{\Lambda}\Lambda$ case. This finding suggests a difference in the production mechanism and/or the final-state interaction of the respective hyperon-antihyperon systems and, possibly, direct evidence of strong coupling to K^* exchange. Finally, no resonance structure is required to explain the total cross section data within the statistics and over the limited excess energy region studied.

ACKNOWLEDGMENTS

The members of the PS185 Collaboration thank the LEAR accelerator team for the excellent preparation of the antiproton beam. We also gratefully acknowledge financial and material support from the German Bundesministerium für Bildung und Forschung, the Swedish Natural Science Research Council, the United States Department of Energy under Contract No. DE-FG02-87ER40315, and the United States National Science Foundation under Contract No. NSF PHY-93-10871.

[1] P. D. Barnes *et al.*, Phys. Lett. B **229**, 432 (1989).
[2] P. D. Barnes *et al.*, Phys. Lett. B **331**, 203 (1994).
[3] M. Kohno and W. Weise, Phys. Lett. B **179**, 179 (1986).
[4] I. S. Shapiro, Phys. Rep., Phys. Lett. **35C**, 129 (1978).
[5] J. Carbonell, K. V. Protasov, and O. D. Dalkarov, Phys. Lett. B **306**, 407 (1993).
[6] P. D. Barnes *et al.*, Phys. Lett. B **246**, 273 (1990).
[7] P. D. Barnes *et al.*, Phys. Rev. C **54**, 2831 (1996).
[8] J. Badier, A. Bonnet, P. Briandet, and B. Sadoulet, Phys. Lett. **25B**, 152 (1967).
[9] M. Kohno and W. Weise, Nucl. Phys. **A479**, 433c (1988).
[10] J. Haidenbauer *et al.*, Phys. Rev. C **46**, 2516 (1992).
[11] Application Software Group, Computing and Networks Division, GEANT Detector Description and Simulation Tool, CERN, Geneva, Switzerland, 1993.
[12] Brian Bunker, Ph.D. thesis, University of Illinois at Urbana-Champaign, 1998.
[13] Timothy D. Jones, Ph.D. thesis, University of Illinois at Urbana-Champaign, 1996; Jörg Hauffe, Ph.D. thesis, Universität Erlangen-Nürnberg, 1999.
[14] F. Tabakin, R. A. Eisenstein, and Y. Lu, Phys. Rev. C **44**, 1749 (1991).
[15] P. D. Barnes *et al.*, Phys. Lett. B **189**, 249 (1987).
[16] P. D. Barnes *et al.*, Nucl. Phys. **A526**, 575 (1991).
[17] P. D. Barnes *et al.*, Phys. Rev. C **54**, 1877 (1996).
[18] T. Johansson *et al.*, Nucl. Phys. **A655**, 173c (1999).